Nanoscale

PAPER

View Article Online
View Journal | View Issue

Cite this: *Nanoscale*, 2026, **18**, 10243

The golden rule to address charge transfer in dibenzenthiols-derivates/gold nanoparticles hybrids

Antonio Cardone, *[a] Maria Losurdo, [b] Giuseppe Valerio Bianco, [c] Stefano Dicorato,[c] Agostina Lina Capodilupo [d] and Maria Michela Giangregorio *[c]

Organic molecule–gold nanoparticles (Au NPs) hybrids based on a luminescent small organic molecule 4,4′-((((5,6-bis((2-hexyldecyl)oxy)benzo[*c*][1,2,5]thiadiazole-4,7-diyl)bis(thiophene-5,2-diyl))bis(methanylylidene))bis(azanylylidene))dibenzenethiol (**BTTh**) and plasmonic Au NPs, with size ranging from 30 to 120 nm, were engineered and compared with layers of **BTTh** on gold film and glass and characterized by spectroscopic ellipsometry, Raman spectroscopy, Photoluminescence (PL) current–voltage (CV) measurements, atomic and Kelvin probe force microscopy. We found that their optical, structural and morphological properties changed with size. Specifically, we found that Au NPs with size ≤70 nm allow formation of uniform **BTTh** monolayers with short and strong Au–S bond promoting charge transfer processes from Au to **BTTh**. Through the construction of the energy levels scheme of **BTTh**–Au NPs hybrids, we discussed the effects of NPs size on the relative energy position between the HOMO–LUMO levels of **BTTh** and the work function (WF) and localized surface plasmon resonance (LSPR) of Au NPs, rationalizing the charge transfer process occurring between Au NPs and **BTTh**. These findings provided a versatile tool to design appropriate combinations of organic molecules–metal nanoparticles aimed to hybrid materials for optoelectronic applications.

Received 17th December 2025,
Accepted 4th April 2026

DOI: 10.1039/d5nr05316a

rsc.li/nanoscale

1. Introduction

Hybrid systems consisting of organic molecules–metal nanoparticles (NPs) provide a powerful approach for bottom-up design of novel architectures,[1–5] also combining synergetic properties exceeding the functionality of the individual components and achieving advanced materials with enhanced and/or multiple functionalities stemming from unusual materials combinations.

The development of such hybrid systems evolved following the extensive progress in synthetic control achieved for both metal nanocrystals, yielding systems with well-defined shapes/size and compositions, and organic molecules yielding a fine tuning of their functionality at the molecular level, of their electronic and optical properties, as well as solubility and solid state aggregation (thickness, the degree of order, and morphology).[6–8] These achievements provided the background for the development of organic molecule–metal NPs hybrids.

Organic molecule–metal NPs hybrids have been investigated in recent years for different applications such as Organic Light Emission Diodes (OLEDs), Organic Field Effect Transistors (OFETs), bulk-heterojunction and dye-sensitized solar cells, chemical sensors.[9–13] While some of these applications are already in the market (OLEDs, OFETs), some others are still far from real applications in spite of the enormous strides in efficiency registered in the last decades (bulk heterojunction solar cells).[14] Improving the efficiency of such devices requires control over size, shape and composition of metal NPs, the chemical nature and electronic structure of the organic building blocks, the degree of order of the organic molecules in the active layer, the presence of dopants and impurities or the nanoscale morphology of the organic films, and finally, the right degree of interaction between the two components.[15]

The energy level alignment (ELA) in these hybrid systems and in particular, the energy-level offsets between the highest occupied molecular orbitals (LUMOs) of the organic molecule and the work function of the metal play a crucial role in deter-

[a]*Institute of Chemistry of OrganoMetallic Compounds, Italian National Council of Research, CNR, Via Orabona, 4, 70126 Bari, Italy. E-mail: antonio.cardone@cnr.it*
[b]*Institute of Chemistry of Condensed Matter and of Technologies for Energy, CNR-ICMATE, Corso Stati Uniti 4, Padova, Italy. E-mail: maria.losurdo@cnr.it*
[c]*Institute of Nanotechnology, Italian National Council of Research, CNR, Via Orabona, 4, 70126 Bari, Italy. E-mail: mariamichela.giangregorio@cnr.it, giuseppevaleriobianco@cnr.it, stefano.dicorato@cnr.it*
[d]*Institute of Nanotechnology, Italian National Council of Research, CNR, Campus Ecotekne, Via Lecce-Monteroni, 4, 73100 Lecce, Italy. E-mail: agostina.capodilupo@nanotec.cnr.it*

mining the device performance, because they affected the charge injection efficiency and the probability of radiative recombination. The optimization of this offset by choosing the right coupling between NP (the right size) and the organic material with the most suitable energy levels can lead to more efficient exciton dissociation and charge generation.[16–19]

In this contribution, we investigate hybrid systems composed by gold nanoparticles (Au NPs) and a thiol-functionalized luminescent small organic molecule 4,4′-((((5,6-bis((2-hexyldecyl)oxy)benzo[*c*][1,2,5]thiadiazole-4,7-diyl)bis(thiophene-5,2-diyl))bis(methanylylidene))bis(azanylylidene))dibenzenethiol, labelled as **BTTh**, promising candidates for high performance organic-based optoelectronic devices.[20–29]

Plasmonic Au NPs show localized surface plasmon resonance (LSPR) in the visible range, tunable by their size and shape. Moreover, they absorb and scatter light order of magnitudes stronger than other materials.[30] Au NPs are also non-toxic, highly photostable and can efficiently bind biomolecules.[31,32]

The position, width and intensity of the LSPR band are strongly dependent on nanoparticle size, shape, and dielectric environment, providing tunable optical responses that have been exploited in sensing, spectroscopy and light–matter interaction studies.[33–35]

The integration of gold nanoparticles with organic semiconductors and inorganic materials has been intensively explored for enhanced light harvesting and charge transfer applications. In plasmonic heterostructures, the LSPR of AuNPs not only extends light absorption into the visible region but also facilitates hot-electron generation and transfer to adjacent semiconductor or molecular acceptor states, promoting photocatalytic and photoelectronic processes.

Furthermore, the ad-hoc functionalization of the conjugated backbone of **BTTh** with –SH end groups allows to realize an organic ligand able to efficiently binding Au. With this aim, we tailored and prepared the **BTTh** molecule by a simple and versatile synthetic protocol.

In this work we report a straightforward strategy for preparing **BTTh**–Au NPs hybrids based on Au NPs of different size (30, 70 and 120 nm). We investigated **BTTh**–Au NPs hybrids by atomic force microscopy (AFM), ellipsometry, CV measurements, Raman spectroscopy and PL measurements. We compared **BTTh**–Au NPs hybrids with layers of **BTTh** on Au film and glass. CV and ellipsometric characterizations provided valuable insights into properties of **BTTh**–Au NPs hybrids, including spectra of refractive index and extinction coefficient, energy gap, HOMO–LUMO levels, charge transfer, thickness of **BTTh** and localized surface plasmon resonance (LSPR) of Au NPs. Additionally, chemico-structural properties, such as Au–S and S–H bonds, surface roughness and the density of the organic molecule layered on Au NPs were investigated by Raman spectroscopy and AFM. Noteworthy, based on the collected data, a schematic illustration of the energy levels in **BTTh**–Au NPs hybrids as a function of Au NPs size was constructed. Through the relative positions of HOMO–LUMO energy levels of **BTTh**, the LSPR and work functions (WFs, from our previous work)[36] of NPs, we can provide insight into the charge transfer between Au NP_S and **BTTh**, rationalizing why it occurs when Au NPs with size below 70 nm are used to realize the **BTTh**–Au NPs hybrids.

2. Experimental

Synthesis

All chemicals were purchased from commercial sources and used without further purification. All reactions sensitive to air were carried out under a nitrogen atmosphere with anhydrous solvents, distilled immediately prior to use. THF and toluene were distilled from sodium and benzophenone, ethanol was distilled from 4 Å molecular sieves. Column chromatography was performed using silica gel 60, 40–63 μm. Silica gel 60 F254 aluminum sheets were used for analytical TLC. FT-IR spectra were measured on a spectrophotometer using dry KBr pellets. ^{1}H and ^{13}C NMR spectra were recorded in $CDCl_3$ on a 400 MHz spectrometer at 400 MHz and 101 MHz, respectively. The residual $CHCl_3$ signals at 7.26 ppm and 77.0 ppm were used as the standard for ^{1}H and ^{13}C NMR, respectively. Elemental analyses were done by an elemental analyzer. Melting points were determined on a Gallenkamp capillary melting point apparatus.

Synthesis of 5,5′-(5,6-bis(2-hexyldecanoxy)benzo[*c*][1,2,5]thiadiazole-4,7-diyl)bis(thiophene-2-carbaldehyde) 3. In a 100 mL three-necked round-bottom flask, under a nitrogen atmosphere, were added **1** (1.3 g, 1.68 mmol), **2** (1.4 g, 3.50 mmol), $Pd(PPh_3)_4$ (63 mg, 0.05 mmol) and dry toluene (30 mL). The resulting mixture was refluxed overnight, then cooled at room temperature, quenched with water and extracted with ethyl acetate. The solvent was removed under a reduced pressure, and the crude product was dissolved in ethyl acetate and treated with aq. 40% KF solution. The organic layer was dried over anhydrous Na_2SO_4 and the solvent removed at a reduced pressure. The crude residue was extracted in a Soxhlet apparatus with hexane and after separation from the solvent, the pure product **3** was recovered as a dense red-brown liquid (0.98 g, 70% yield,). ^{1}H NMR (400 MHz, $CDCl_3$) δ 10.02 (s, 2H), 8.36 (d, J = 4.0, 2H), 7.86 (d, J = 4.0, 2H), 4.00 (d, J = 6.6, 4H), 1.93 (quint, J = 6.2, 2H), 1.50–1.15 (bs, 48H), 0.87 (t, J = 6.8, 6H), 0.86 (t, J = 6.8, 6H). ^{13}C NMR (101 MHz, $CDCl_3$) δ 182.95, 153.81, 150.28, 144.04, 142.92, 135.12, 131.56, 117.71, 79.05, 38.84, 31.73, 31.68, 30.96, 30.95, 29.89, 29.54, 29.45, 29.17, 26.60, 26.56, 22.50, 13.93, 13.92. FT-IR (KBr): ν 2955 (s), 2925 (s), 2855 (s), 1671 (s), 1464 (s), 1442 (s), 1420 (s), 1287 (s), 1226 (s), 1209 (s), 1093 (m), 1224 (s), 955 (m), 913 (m), 673 (m) cm^{-1}. Elemental analysis calcd for $C_{48}H_{72}N_2O_4S_3$: C, 68.86; H, 8.67; N, 3.35; S, 11.49; found: C, 68.95; H, 8.88; N, 3.42; S, 11.41.

Synthesis of 4,4′-((((5,6-bis((2-hexyldecyl)oxy)benzo[*c*][1,2,5]thiadiazole-4,7-diyl)bis(thiophene-5,2-diyl))bis(methanylylidene))bis(azanylylidene))dibenzenethiol (BTTh). In a 100 mL three-necked round-bottom flask, under a nitrogen atmosphere, compound **3** (0.5 g, 0.6 mmol), 4-aminothiophenol (0.21 g,

1.7 mmol) and dry ethanol (10 mL) were added. The resulting mixture was refluxed overnight, then cooled at room temperature. The precipitate was filtered and washed with ethanol to yield the pure product as a dark-red solid (0.61 g, 98% yield). Mp. 95–96 °C. ^{1}H NMR (400 MHz, $CDCl_3$) δ 8.61 (s, 2H), 8.26 (d, J = 3.8, 2H), 7.06–705 (m, 5H), 7.34–7.27 (bs, 1H), 7.25–7.13 (m, 4H), 4.0 (d, J = 6.4, 4H), 1.95 (quint, J = 6.1, 2H), 1.70–1.10 (m, 48H), 0.90–0.77 (bs, 12H). ^{13}C NMR (101 MHz, $CDCl_3$) δ 153.66, 152.94, 151.07, 150.78, 143.75, 139.02, 134.49, 131.80, 131.37, 130.52, 129.63, 121.90, 121.87, 117.86, 78.94, 77.20, 39.05, 31.92, 31.89, 31.21, 30.12, 29.76, 29.67, 29.38, 26.85, 26.82, 22.67, 14.10. FT-IR (KBr): ν 2921 (s), 2917 (s), 2852 (s), 1605 (s), 1572 (s), 1445 (s), 1415 (m), 1379 (m), 1351 (m), 1330 (m), 1282 (s), 1191 (s), 1094 (m), 1019 (s), 954 (m), 811 (s), 535 (s) cm^{-1}. Elemental analysis calcd for $C_{60}H_{82}N_4O_2S_5$: C, 68.53; H, 7.86; N, 5.33; S, 15.24; found: C, 68.61; H, 7.93; N, 5.36; S, 15.20.

Au film and NPs deposition

Au films and NPs supported on c-Si (111) were deposited by sputtering an Au target by a radiofrequency (rf = 13.56 MHz) Ar plasma.[37] The sputtering time was used as parameter to obtain NPs with size of 30 nm, 70 nm and 120 nm.

SAMs formation

SAMs of **BTTh** on Au NPs were formed using the Au NPs supported on c-Si (111). Before **BTTh** functionalization, Au NPs were annealed for 3 h at 250 °C in ultra-high vacuum, in order to reduce both adventitious contaminants and Au surface roughness. SAMs were formed by dipping supports for 1 h in 2 μM solutions of **BTTh** in $CHCl_3$ at 25 °C (controlled by a thermostatic bath). Samples were subsequently rinsed with $CHCl_3$ and dried under a N_2 stream.

Characterization

CV measurements. The electrochemical properties of **BTTh** were investigated by cyclic voltammetry (CV) (Fig. 1) at room temperature in CH_2Cl_2 solution, with tetrabutylammonium hexafluorophosphate ($TBAPF_6$) (0.1 M) as supporting electrolyte and with a scan rate of 50 mV s^{-1}. A typical trielectrode configuration with ferrocene as the internal standard was used to perform the measurements. The HOMO level of **BTTh** was quantified.

Optical, morphological and structural characterization of BTTh–Au NPs/film hybrids. The optical response of the hybrid systems was investigated by spectroscopic ellipsometry (SE). Measurements were carried out at an incidence angle of 70° to investigate the optical transitions of **BTTh** and to detect the plasmon resonance behavior of the **BTTh**–Au NPs hybrids using a phase-modulated spectroscopic ellipsometer (UVISEL, HORIBA) in the energy photon range 0.75–6.50 eV with a resolution of 0.05 eV.

In order to derive the spectral dependence of the refractive index, n, and extinction coefficient, k, (n + ik), of **BTTh** from the measured SE spectra of the pseudo-dielectric function, $\langle\varepsilon\rangle = \langle\varepsilon_1\rangle + \langle\varepsilon_2\rangle$, spectra were measured for **BTTh** films on Au film

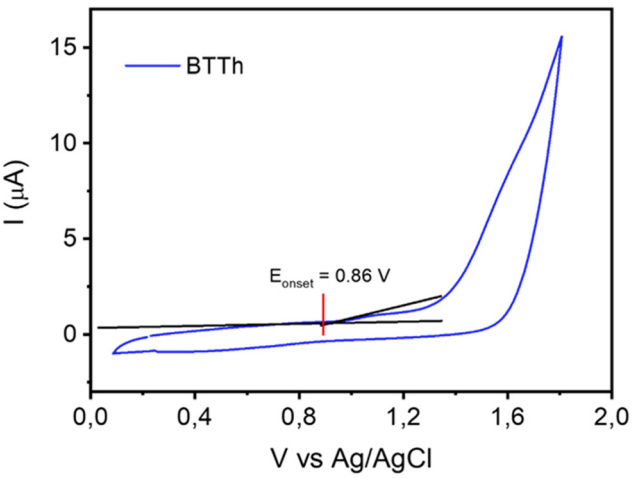

Fig. 1 Cyclic voltammograms of **BTTh** in CH_2Cl_2 solution (c = 1 × 10^{-3}) [$TBAPF_6$] 0.1 M, scan rate of 50 mV s^{-1}. The oxidation onset potential ($E_{onset(ox)}$) used for the determination of the HOMO energy level is indicated. $E_{HOMO} = -(E_{onset(ox1)} - E_{1/2(Fe)} + 5.16)$ (eV). $E_{LUMO} = E^g_{opt} - E_{HOMO}$.

and analyzed using a two-layer isotropic model consisting in substrate/organic film/air. The energy dispersion of the optical constants of the **BTTh** was modeled using an ensemble of Lorentzian oscillators, according to the equation:

$$N^2 = (n + ik)^2 = \varepsilon = \varepsilon_1 + i\varepsilon_2 = \varepsilon_\infty + \sum_j \frac{A_j \omega_j{}^2}{\omega_j{}^2 - \omega^2 - i\gamma_j \omega} \quad (1)$$

where ε_∞ is the high frequency dielectric constant, ω_j, γ_j and A_j are the frequency, width and strength, respectively, of the j-th oscillator, with each oscillator representing an optical transition, whose energy and broadening was determined by fitting routine.

Four Lorentzian oscillators were considered on the basis of all possible electronic transitions expected in the investigated photon energy range.

For the analysis of data, a regression approach was used, building a model representing the sample structure and calculating ε for that model for M photon energies. The calculated values are compared with the measured data in a fit routine that, using a Levenberg–Marquardt algorithm by varying film thickness and optical constants, minimizes the mean squared error, χ^2, defined as,

$$\chi^2 = \frac{1}{2M - P - 1} \sum_{i=1}^{M} \frac{\left(\langle\varepsilon_{1,exp}\rangle - \langle\varepsilon_{1,cal}\rangle_i\right)^2}{\sigma_{1,i}{}^2} + \frac{\left(\langle\varepsilon_{2,exp}\rangle - \langle\varepsilon_{2,cal}\rangle_i\right)^2}{\sigma_{2,i}{}^2} \quad (2)$$

where M is the total number of data points, P is the number of fitted parameters, $\varepsilon_{1,exp}$, $\varepsilon_{1,cal}$, $\varepsilon_{2,exp}$, $\varepsilon_{2,cal}$, representing the experimental and calculated real and imaginary parts of the pseudo-dielectric function, and i is the error of each measured quantity.

Film thickness and oscillators parameters were the ellipsometric fitting variables.

SE was also demonstrated to be suitable in the case of the optical analysis of Au NPs through the monitoring of the localized surface plasmon resonance (LSPR) and of its modification upon the interaction with the organic molecule. Once known the parametric oscillator models for the Au NPs and the **BTTh**, they were used as input to derive **BTTh** thickness and optical response in hybrids, analyzing them with a four-layer model (Si/AuNPs/**BTTh**/air). The change in the LSPR position and width of Au NPs in hybrids was investigated directly from experimental data. The validity of these results on the **BTTh** optical constants and optical thickness (OT) has been confirmed statistically on a large number of samples.

The **BTTh** optical gap was calculated plotting $(\alpha h\nu)^2$ as a function of energy.

Raman and PL spectra were collected using a LabRAM HR Horiba–Jobin–Yvon spectrometer with 473 nm laser sources under ambient conditions (laser power 1 mW). The use of the laser at 473 nm was necessary to extend the energy range of PL measurements to 2.6 eV in order to include **BTTh** optical emissions. The excitation laser beam is focused through a 50× LWD optical microscope (N.A. = 0.5, spot size of ~1 μm^2 and depth of laser focus of ~7.6 μm). In order to correctly quantify the magnification of signals of molecules interacting with the surface of plasmonic nanostructures, all sample collection and handling conditions were kept invariant throughout all the measurements, *i.e.* the laser power, accumulation time and exposure time.

Non-contact intermittent mode atomic force microscopy (AFM) was used for characterizing morphology and RMS (root mean square) of **BTTh** on glass, and Au NPs and Au film before and after **BTTh** functionalization using an AutoProbe CP Thermomicroscope. A high aspect ratio probe-super sharp tip with a radius of curvature of 2 nm (ESP Series Probes-VEECO) was used to reduce the convolution effect of the tip on the lateral size of NPs.

The work functions of the Au NPs were measured by Kelvin probe electrical force microscopy (KPFM) through the measurement of the local variation of the surface potential (SP). All details are reported in our previous paper.[36]

3. Results and discussion

Synthesis of BTTh

The small organic molecule **BTTh** was synthesized following the retrosynthetic route in Scheme 1. Compounds **1** and **2** were prepared following the literature procedure.[31,38,39] Compound **3** was prepared following the Stille synthetic protocol by reacting reagents **1** and **2**, in the presence of $Pd(PPh_3)_4$ as the catalyst, in toluene at reflux. After purification by Soxhlet extraction

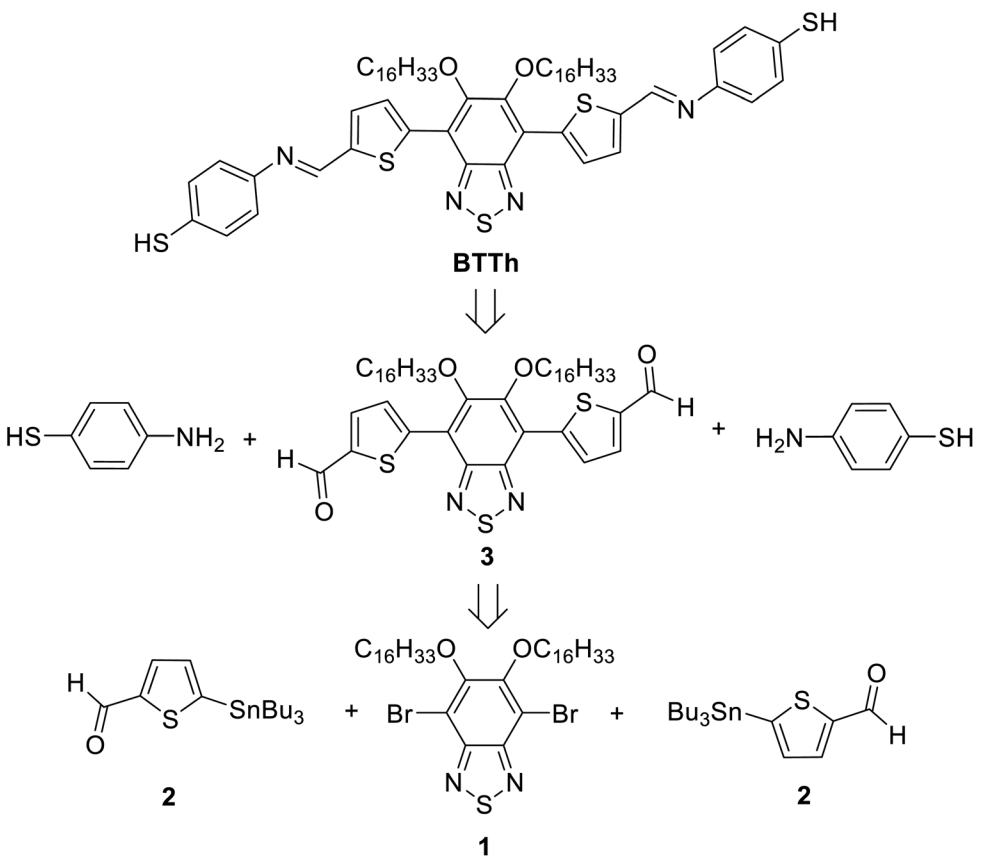

Scheme 1 Retrosynthetic route to organic molecule **BTTh**.

with hexane and following separation from the solvent, compound **3** was obtained as a dense red-brown liquid. Finally, by reacting compound **3** with 4-aminothiophenol in dry ethanol at reflux, compound **BTTh** was obtained in almost quantitative yield as a dark-red powder. Compound **BTTh** precipitates in the reaction medium and can be purified by a simple filtration and following washing with ethanol.

CV characterization

According to the equation $E_{HOMO} = -(E_{onset(ox1)} - E_{1/2(Fe)} + 5.16)$ (eV), the HOMO level was quantified as −5.42 eV, as shown in Fig. 1. The LUMO level of **BTTh** was derived according to $E_{LUMO} = E_g^{opt} + E_{HOMO}$ (eV), where E_g^{opt} is the optical gap, estimated from ellipsometric analysis of thin films.

Morphological characterization of BTTh–Au NPs/film hybrids

In Fig. 2 AFM images 2D 3 μm × 3 μm of **BTTh** deposited on (a) glass, (c) Au film and (d–f) Au-NPs of different size are reported. **BTTh** forms on glass agglomerates with high RMS, ~11 nm (Fig. 2a and b), while on Au film the coverage is homogenous with RMS = 1.1 nm (Fig. 2b and c) as a consequence of the anchoring of **BTTh** through the S–H group to gold. The RMS of hybrids increases from 2 nm to 12 nm with increasing NPs size (Fig. 2b). 3D 500 nm × 500 nm topographical images of **BTTh** on Au NPs (Fig. 2d′–f′) compared with images of AuNPs before **BTTh** deposition (Fig. 2h′–l′) highlighted that the RMS and morphology of hybrids are not significantly altered after **BTTh** deposition on NPs, suggesting conformal anchoring of **BTTh** to Au NPs by the –SH end groups.

The contrast in morphology between **BTTh** on glass and on Au (NPs and film) clearly indicated the important role of the –SH group anchoring the gold in addressing the uniform organic layer.

Ellipsometric characterization of BTTh–Au NPs/film hybrids

Optical and structural properties of **BTTh** films on glass and Au NPs/film were investigated by ellipsometry. Fig. 3a shows the spectra of the refractive index and extinction coefficient derived for the **BTTh** layer on Au film with an estimated optical thickness (OT) of 42.3 ± 1.7 nm. The spectrum of the extinction coefficient shows four main transitions that can be associated to the molecule structure, namely the transition at 2.35 eV (~528 nm) corresponding to the n–π* transition,[40] at 3.23 eV (~384 nm) due to the π–π* transitions of its conjugated backbones, at 4.80 eV (~258 nm) and 6.21 eV (~200 nm) due to benzene-derivates. By the Tauc-plot of $(\alpha h\nu)^2$ *vs.* energy, in

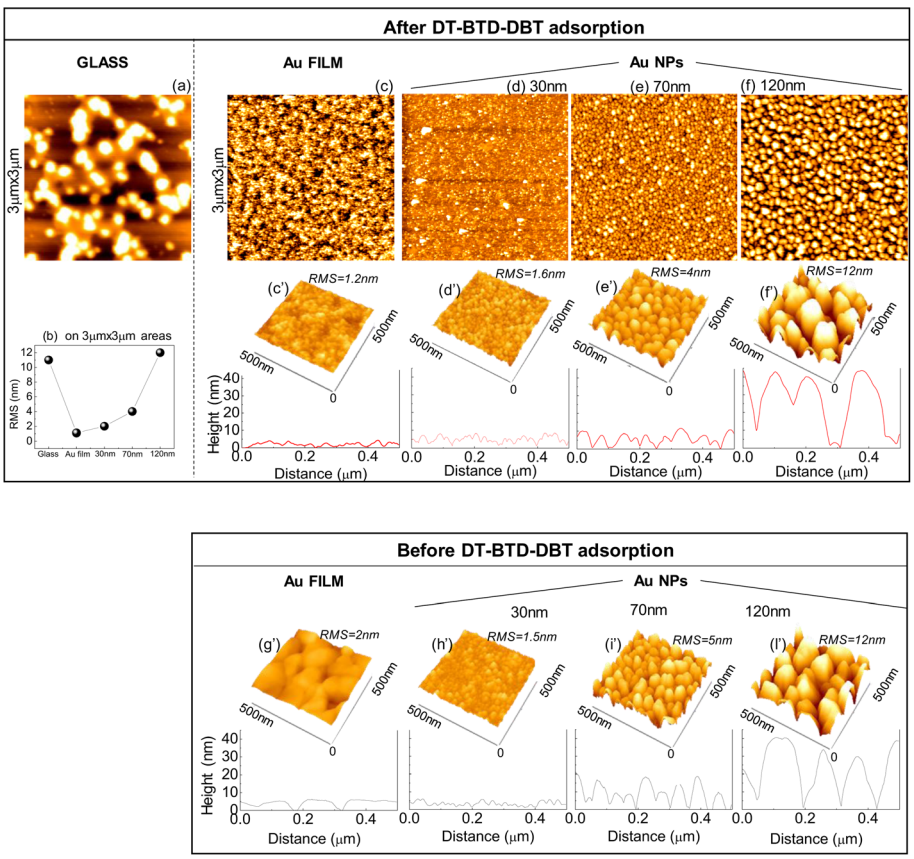

Fig. 2 AFM images 2D 3 μm × 3 μm of **BTTh** on (a) glass, (c) Au film and (d–f) 30-, 70-, 120 nm Au NPs. (b) Evolution of the RMS calculated on 2D 3 μm × 3 μm areas for the different samples. 3D 500 nm × 500 nm topographical images of Au film and Au NPs after (c′–f′) and before (g′–l′) **BTTh** deposition. Representative line profiles on 3D 500 nm × 500 nm images are also shown, all in the same scale from 0 to 54 nm. RMS data are also reported. 2D 3 μm × 3 μm and 3D 500 nm × 500 nm images have the same vertical scale, that is, respectively, 0–82.27 nm and 0–62 nm.

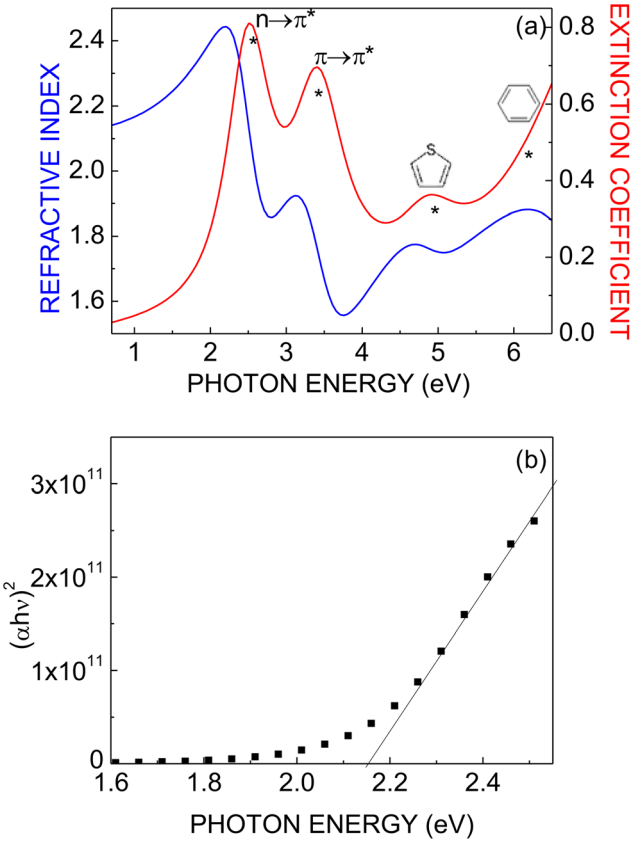

Fig. 3 (a) Spectra of the refractive index (blue line) and extinction coefficient (red line) of **BTTh**. The main transitions and the corresponding attributions are indicated by (*) on the spectrum of extinction coefficient. (b) $(\alpha h\nu)^2$ *vs.* energy for the evaluation of the gap.

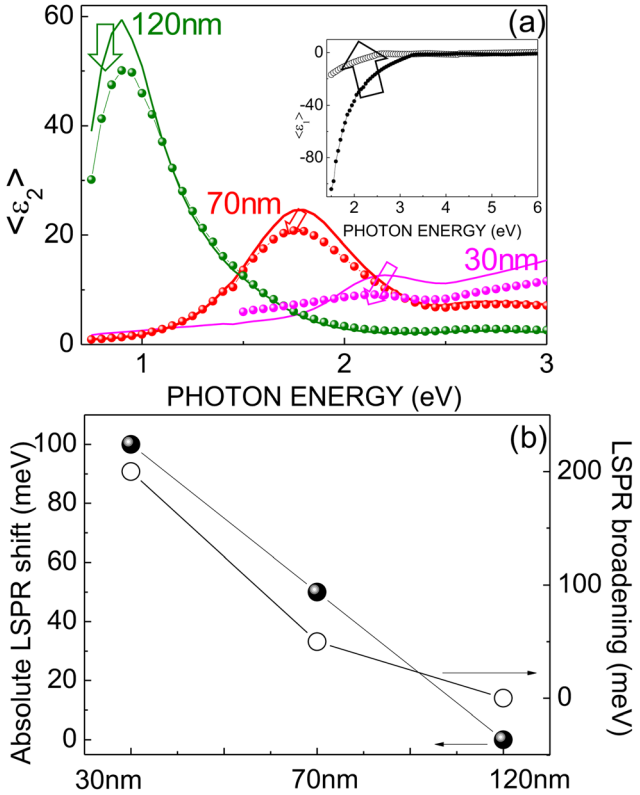

Fig. 4 (a) Spectra of the imaginary part of the pseudo-dielectric function, $\langle\varepsilon_2\rangle$, in the energy range 0.75–3 eV, of Au NPs with different size, 30, 70 and 120 nm, before (continuous line) and after (scattered filled points) **BTTh** anchoring. The $\langle\varepsilon_1\rangle$ spectra of Au film before and after functionalization is also shown for comparison as inset. (b) Evolution of the change in the LSPR energy position and broadening after functionalization as a function of NPs size.

Fig. 3b, an optical gap of 2.16 ± 0.04 eV was estimated for **BTTh** (useful parameter for the construction of the energetic scheme in hybrid systems).

Fig. 4a shows spectra of the imaginary part of the pseudodielectric function, $\langle\varepsilon_2\rangle$ of 30, 70 and 120 nm Au NPs, before (continuous line) and after (scattered filled points) **BTTh** anchoring. Bare 30-, 70- and 120 nm Au NPs have LSPR at 2.15 eV, 1.65 eV and 0.9 eV, respectively. After anchoring a different LSPR red-shift and broadening is experimentally observed. Specifically, we only found a LSPR red-shift and broadening upon **BTTh** functionalization of 30 and 70 nm Au NPs. No LSPR shift and broadening are measured for 120 nm Au NPs after **BTTh** anchoring.

Generally, the LSPR energy red-shift observed in **BTTh**–Au NPs hybrids is due to the combination of two factors,[41,42] *i.e.*, (i) the increase of the local refractive index by the backbone of the molecule surrounding the AuNPs; (ii) the change in the electron density of AuNPs due to the electron withdrawing capabilities of thiols. Thiols are more electronegative than gold,[43] so, it is expected that thiols withdraw electrons from the AuNPs.

Therefore, Fig. 4a showed that **BTTh**–Au NPs hybrids with size ≤70 nm yielded films with high refractive index indicative of a dense molecular packing[44] and showed reduction of the density of free electrons[43] due to the charge transfer. On the contrary, **BTTh** on 120 nm AuNPs hybrids showed a low molecular packing and no charge transfer occurred.

The LSPR broadening is indicative of *via* radiative and non-radiative decay channels and charge transfer from AuNPs to **BTTh** molecule.[45–47] For 120 nm-AuNPs after functionalization with **BTTh** the LSPR broadening does not change significantly while for NPs ≤70 nm it increased due to decay channels and charge transfer processes.

The decrease of the real part, $\langle\varepsilon_1\rangle$ of the pseudodieletcric function of Au film after its functionalization with **BTTh** is indicative of the electron transfer of electron from Au to **BTTh** as discussed in ref. 36. From the analysis of the ellipsometric spectra, average **BTTh** optical thickness values of 32 ± 5 Å on 30 nm and 70 nm Au NPs and 62 ± 5 Å on 120 nm Au NPs and on Au film have been determined.

Considering for **BTTh** a molecular length in the range 10–25 Å (measured by the CHEM3d Embed software) depending on the *cis* and *trans* configuration respect to the benzothiadiazole and on the spatial configurations of the aliphatic ether chains and the S–Au bond length of ≈2 Å, a **BTTh** monolayer is formed on 30 nm- and 70 nm-Au NPs.

Photoluminescence and Raman measurements of BTTh–Au NPs/film hybrids

Fig. 5 shows normalized PL spectra of Au NPs in the energy range 1.8–2.5 eV, before (filled areas) and after (continuous lines) **BTTh** adsorption compared with PL spectrum of **BTTh** on glass (black line) and Au film (grey line).

The PL spectra of **BTTh** on glass (black line) and Au film (grey line) show one main band at ~2.34 eV (indicated as B), and a wide shoulder in the range 2.17–2.3 eV (indicated as B′).

When **BTTh** is anchored on Au NPs, PL spectrum becomes more complex with the appearance of two additional bands at ~1.98 eV (626.16 nm) (C-band) and at ~2.12 eV (584.81 nm) (D-band) due to NPs that are added to the E band of Au film at ~2.4 eV. C and D bands in Au NPs are due to interband (d–sp) transitions between energy states sp of conduction band and d of valence band. According to the solid state model of the gold metal, luminescence is produced by the radiative recombination of electron–hole pair between the 5d- and 6sp-bands, which corresponds to the E band. In noble metal nanoparticles, bands split into a series of energy levels due to the quantum size effect.[48–57] The relationship between level spacing (δ) and particle size is given by $\delta \propto 1/d^3$, where d is the particle size of nanoparticles. So, more transitions from discrete valence states to excited states take place in the Au NPs, generating additional bands, C at ~1.97 eV and D at ~2.13 eV, at energy lower than the E band. Increasing the NP size the intensity of both the C- and D-bands decreases and their broadening increases while the E-band intensity increases and strongly blue-shifts.

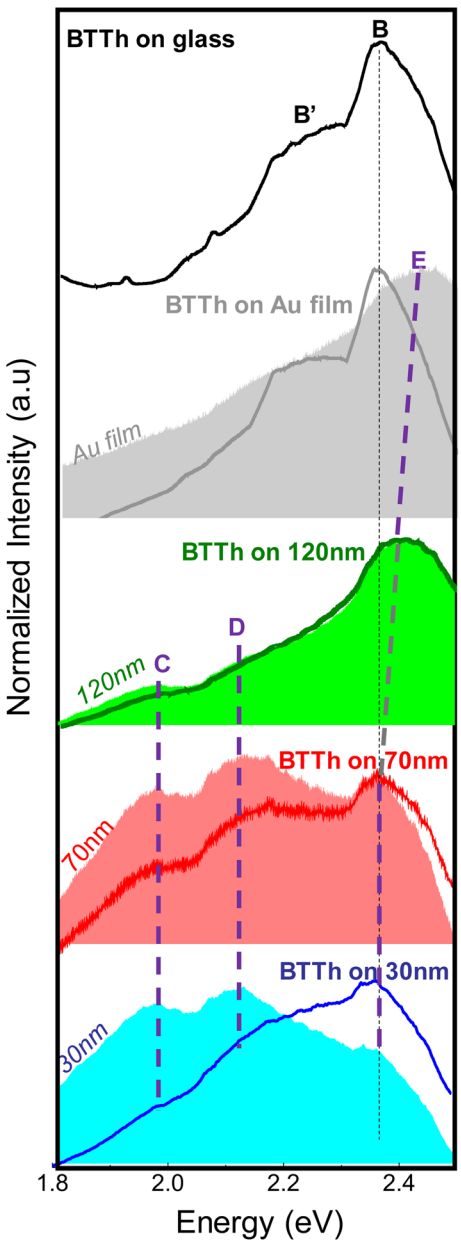

Fig. 5 Normalized PL spectra on glass and Au NPs of different size before (filled areas) and after (continuous lines) adsorption of **BTTh**. The violet dotted lines indicates the position of the C, D and E of bare Au NPs and film while B band position of **BTTh** is indicated by a black dotted line.

PL spectrum of **BTTh**–30 nm Au NPs hybrid (blue line) shows that the C and D bands of Au NPs are broad and low intense and the B and B′ emission bands of **BTTh** predominate, while the E band of NPs overlap the B band of **BTTh**. PL spectrum of **BTTh**–70 nm Au NPs hybrid (red line) shows that the C and D bands of Au NPs are more evident as well as the B and B′ bands of **BTTh**. The E band of NPs continues to overlap the B band of **BTTh**.

After **BTTh** adsorption on 120 nm Au NPs (green line), PL spectrum of NPs does not change showing a broad E band at ~2.4 eV (E band), blueshifted with respect to B band, and low intense C and D bands. B and B′ bands of the **BTTh** adsorption are not evident.

In order to investigate the role of –SH end group of **BTTh** in anchoring Au (NPs/film), Raman measurements were performed for **BTTh** layered on glass and Au (NPs/film) in three different ranges, 200–400 cm^{-1}, 600–1800 cm^{-1} and 2000–3000 cm^{-1}. The results are summarized in Fig. 6(a–c).

In the range 200–400 cm^{-1} (Fig. 6a), bands due to Au–S–C and Au–S modes dominate in **BTTh**–Au NPs/Au film hybrids. In particular, we observed Au–S–C bending modes at ~210 cm^{-1}, Au–S radial modes (R) at ~260 cm^{-1} (indicated by yellow area) and tangential modes (T) at ~300 cm^{-1} (indicated by cyan area).[58] The tangential Au–S vibrations are those of the shorter and stronger Au–S bonds while the radially directed Au–S vibrations are those of the longer and weaker bonds. Plotting the ratio between the intensity of tangential (~300 cm^{-1}) and radial (~260 cm^{-1}) modes, I_{tang}/I_{rad}, as shown in Fig. 7a, we found that going from Au film to NPs, and decreasing NPs size, the I_{tang}/I_{rad} ratio increases from ~0.5 to 2. According to ref. 58–60, this is an indication of the formation of shorter and stronger Au–S bonds in 30 nm-based **BTTh**–Au NPs hybrids.

In the range 600–1800 cm^{-1} (Fig. 6b), bands due to the C–S stretching at ~660 cm^{-1}, the C–S–C deformation mode in the range 690–730 cm^{-1}, the C–S ring stretching in the range 722–880 cm^{-1} and C–N bending modes in the range 520–1022 cm^{-1} are evident.[61–66] Moreover, the signals at ~1080,

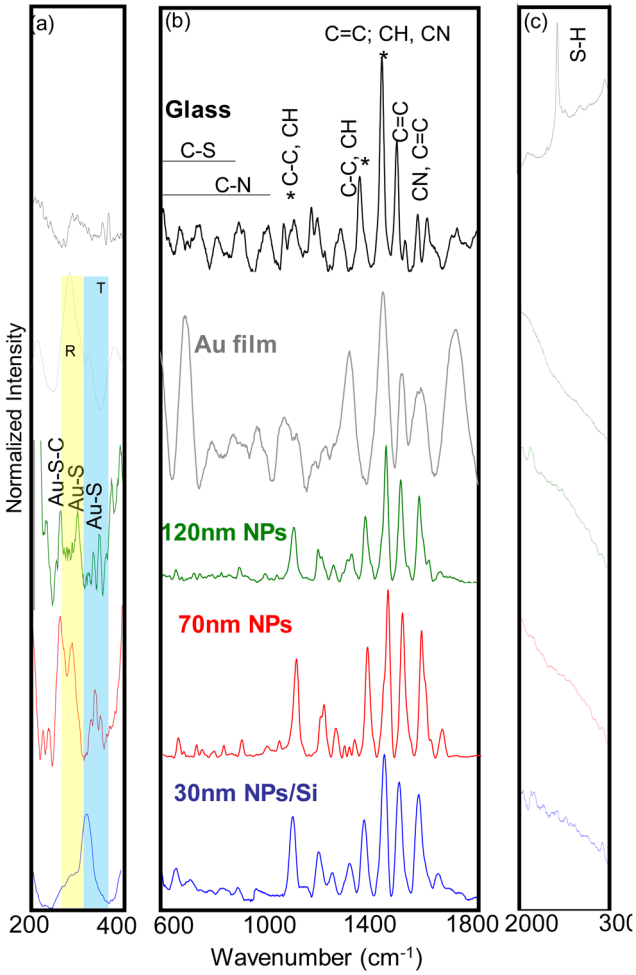

Fig. 6 (a) Raman spectra of **BTTh** on glass (black line), Au film (grey line), 120 nm Au NPs (green line), 70 nm Au NPs (red line) and 30 nm Au NPs (blue line), in three different ranges (a) 200–400 cm^{-1} (b) 600–1800 cm^{-1} and (c) 2000–3000 cm^{-1}. Band assignments are also indicated. R and T areas in yellow and cyan, respectively, indicate Au–S radial and tangential modes. * indicates bands at 1060, 1350 and 1440 involved in the Raman analysis of ratios shown in Fig. 7b.

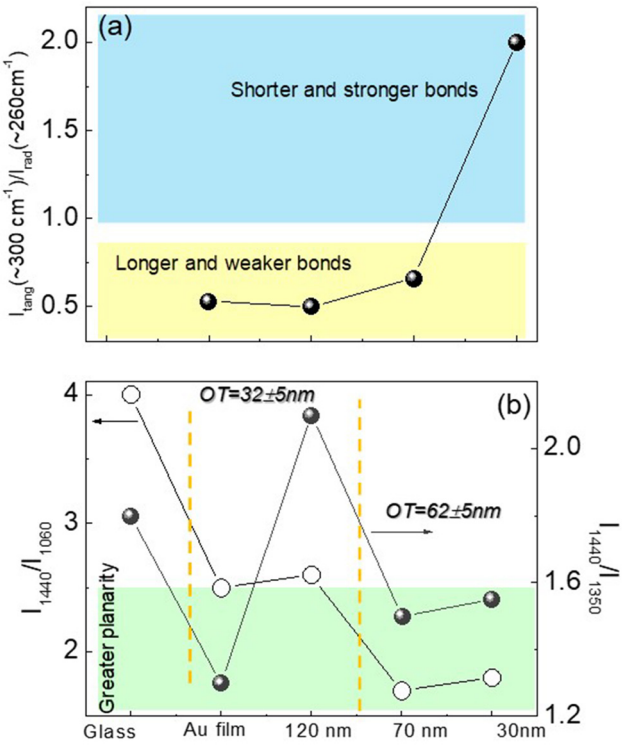

Fig. 7 Evolution of the (a) I_{tang} (~300 cm^{-1})/I_{rad} (~260 cm^{-1}) and (b) I_{1440}/I_{1060} and I_{1440}/I_{1350} ratios as a function of the used substrate. OT indicates the optical thickness from ellipsometry.

1180, 1230, 1300, 1350, 1436, 1500, 1571 and 1650 cm^{-1} can be attributed to main in-plane ring skeleton modes of C–C, C–N and C–H bonds.[61–63,66–71] All spectra are dominated by the band ~1440 cm^{-1} due to (C=C, C–H) and differ in the ratio between the intensity of band at 1060 cm^{-1} (C–C, CH) and 1350 cm^{-1} (C–H, C–C) with respect to band at 1440 cm^{-1}.

Fig. 7b shows the evolution of I_{1440}/I_{1060} and I_{1440}/I_{1350} ratios as a function of the investigated samples. We found that in **BTTh**–30 nm and **BTTh**–70 nm Au NPs hybrids and **BTTh**–Au film, I_{1440}/I_{1060} and I_{1440}/I_{1350} ratios are lower as an indication of the increase of π electron density in C–C bonds, higher intra- and interchain order and packing of **BTTh** chains. On the contrary, in **BTTh** on 120 nm-Au NPs and on glass, higher I_{1440}/I_{1060} and I_{1440}/I_{1350} ratios are observed due to a lower chain packing.[72]

Finally, in the range 2000–3000 cm^{-1} (Fig. 6c), the S–H streching mode from –SH end group dominates the spectrum in the **BTTh** on glass. On the contrary, all hybrids with Au do not show it, supporting the anchoring of S–H end groups of **BTTh** to Au.

Correlating Raman data with the optical thicknesses (OT) from ellipsomerty, we found that **BTTh** arranges on Au film in a thicker layer with more dense molecular packing with respect to **BTTh** on 120 nm AuNPs.

Our results agree with previous Raman studies on oligothiophenes which demonstrated that the increase in C–C intensity (decrease in I_{1440}/I_{1060} and I_{1440}/I_{1350} ratios) is also correlated to an increased charge transfer from C=C bonds, measured in **BTTh**–30 nm Au NPs and **BTTh**–70 nm Au NPs hybrids, according to ellipsometric analysis in par. 3.2.[73]

It should be noted that the observed bond strengthening, as revealed by Raman, arises from static charge transfer between **BTTh** and Au NPs, and it is independent of plasmonic excitations.

Construction of the band structure in BTTh–Au NPs/film hybrids

In order to understand and explain the different electrical behavior of Au NPs as a function of their size in hybrids, the energetic levels of **BTTh** and Au NPs are investigated. Combining LSPR and gap values from ellipsometry, HOMO and LUMO levels from CV measurements with the WFs of Au NPs and Au film measured in a previous paper by Kelvin probe force microscopy (KPFM),[36] the diagram of the energetic levels before (Fig. 8) and after alignment (Fig. 9) can be built.

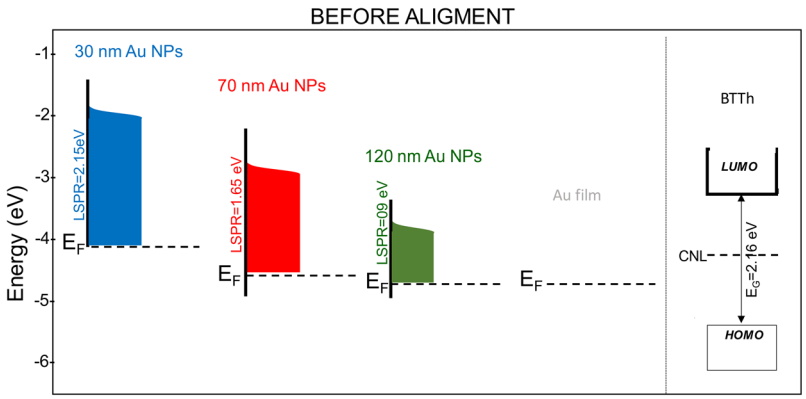

Fig. 8 Band diagrams showing the absolute energy position of the Fermi level and LSPR of Au NPs and film and the HOMO and LUMO of **BTTh** derived by ellipsometry, CV analysis and KPFM.

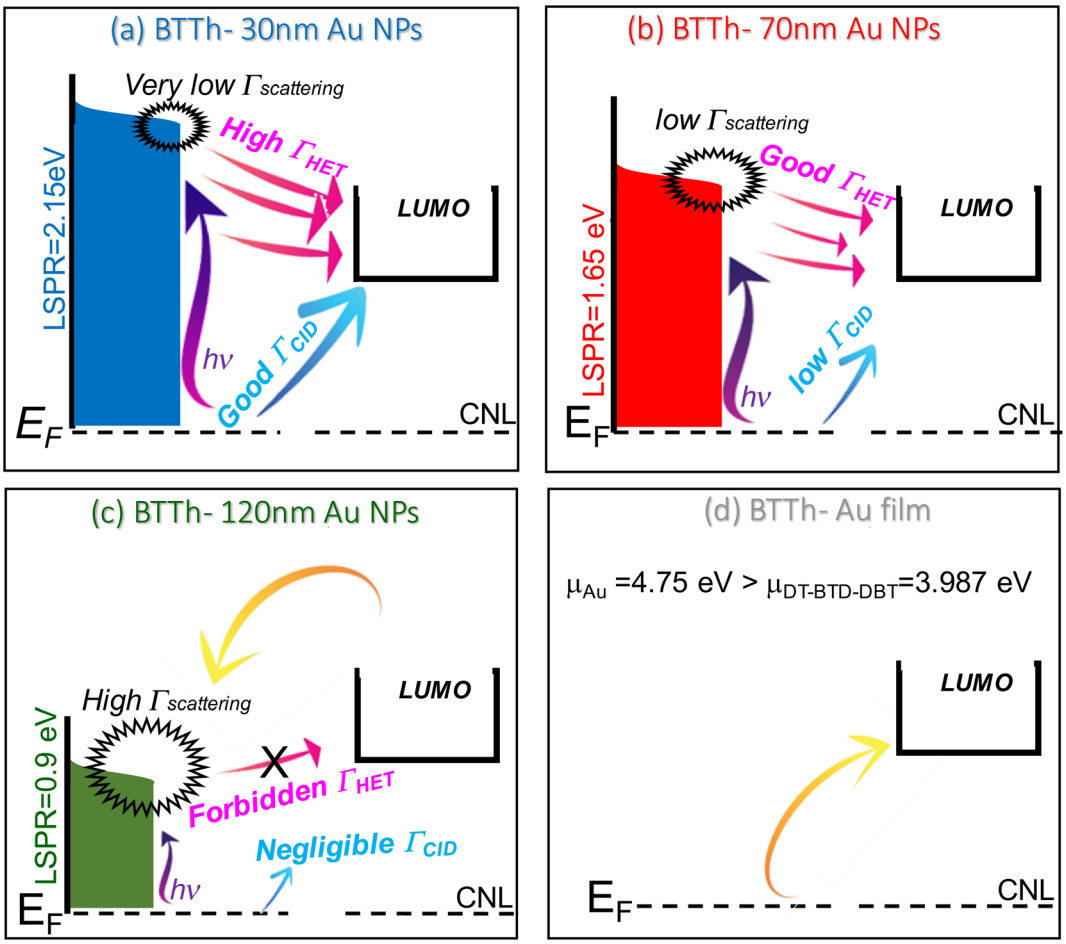

Fig. 9 Energy levels of Au NPs, Au film and **BTTh** after alignment. Representative main radiative and non-radiative decay mechanisms, scattering, $\Gamma_{scattering}$, hot electron transfer, Γ_{HET} and chemical interface damping, Γ_{CID}, involved in a **BTTh**–Au NPs hybrids are also indicated. The different contribution of the three energy transfer mechanisms from NPs as a function of size is represented by the different length of arrows for Γ_{HET} and Γ_{CID} and width of the ☼ symbol for $\Gamma_{scattering}$. The violet arrow indicated the excitation energy while the yellow one the charge transfer direction in **BTTh**–Au film hybrids.

Table 1 HOMO and LUMO energy levels of **BTTh** and LSPR of Au NPs measured by cyclic voltammetry and ellipsometry and WFs of Au film and Au NPs determined by Kelvin probe force microscopy (KPFM) in ref. 36

	BTTh	30 nm Au NPs	70 nm Au NPs	120 nm Au NPs
Homo (eV)	−5.42			
Lumo (eV)	−3.26 ± 0.04			
WF (eV)		−4.06 ± 0.05	−4.63 ± 0.05	−4.75 ± 0.05
LSPR (eV)		2.15 ± 0.05	1.65 ± 0.05	0.90 ± 0.05

In Table 1 we summarized the energy values of HOMO and LUMO levels of **BTTh**, the WFs of Au film and Au NPs with their corresponding LSPR from ellipsometric measurements discussed in par. 3.4.

Since organic molecules generally do not have (quasi-)free electronic charges, we followed the common approach to consider their Fermi level coincident with the so-called charge-neutrality level (CNL).[74–76]

An excited plasmon generated into Au NPs can have three main metal-to-molecule charge-transfer processes, *i.e.* a radiative decay by scattering of electrons at the surface of the AuNP, with a plasmon decay rate $\Gamma_{\text{scattering}}$ (indicated by the ☼ symbol), a non-radiative indirect charge transfer from the SPR states,[77–79] with a decay rate Γ_{HET}, where HET is the hot electron transfer (indicated by fuchsia arrow) and a non-radiative direct interfacial-charge transfer from the Au Fermi level, with a decay rate Γ_{CID} where CID means chemical interface damping (indicated by the cyan arrow).[80] These three processes compete with the quick relaxation of hot electrons *via* electron–electron scattering back to the Fermi level before they can transfer to the molecule, in addition to the decay of plasmons into heat.

The competition between these three photo-induced metal-to-molecule charge-transfer processes in organic molecule–NPs hybrids depend on NPs size and, hence, on the corresponding alignment of the energetic levels of organic molecule and NP.

Specifically, $\Gamma_{\text{scattering}}$ has been demonstrated to occur for Au NPs with size larger than 35–40 nm and becomes significant for 100–130 nm-AuNPs.[81,82]

On the contrary, the contribution of the hot electron transfer, Γ_{HET}, depends on the relative energetic position of SPR with respect to the WF_{Au}–$LUMO_{molecule}$ energy barrier.[82] If the energy of the hot electrons, SPR, is larger than WF_{Au}–$LUMO_{molecule}$, the hot electrons can be efficiently transferred to the conduction band of the molecule. Increasing NPs size, the efficiency of this mechanism is expected to decrease because hot electrons have smaller excitation energies and their number decreases.[80,82]

The chemical interface damping, Γ_{CID}, is a plasmon damping channel, which arises from the direct transfer of hot electrons generated in Au to the LUMO of strongly interacting adsorbate molecules. It is particularly efficient in thiol-functionalized molecules/metal nanoparticle systems, where a strong interaction between them takes place thanks to the capacity of thiol group to covalently bind the gold, causing significant orbital mixing between sulfur and gold atoms.[80,83,84] This process is more efficient than Γ_{HET} because it does not require specific band energy alignment and it does not suffer from electron–electron scattering relaxation back to the Fermi level before they can transfer to molecules from the nanoparticle surface.[85] The contribution of CID predominates in small NPs, with size ≤20 nm.[80,83–86]

Therefore, acting on NP size, the relative contributions of the different damping mechanisms, $\Gamma_{\text{scattering}}$, Γ_{HET} and Γ_{CID}, as shown in Fig. 9, change yielding tailoring of electron transfer in **BTTh**–Au NPs hybrids. Specifically, Au NPs with size 30–70 nm are able to efficiently transfer energy to the molecule thanks to the combination of the three radiative decay mechanisms while in 120 nm Au NPs surface plasmons decay mainly through radiative scattering, the Γ_{HET} is forbidden because SPR is lower than WF_{Au}–$LUMO_{molecule}$ and Γ_{CID} negligible. This explains why the PL spectrum of 120 Au NPs hybrids does not change after **BTTh** absorption not showing its PL bands.

In the case of **BTTh**–Au film hybrids the direction of the electron charge transfer is controlled by the chemical potentials of the two species. The chemical potential of a metal, μ_M, and an organic molecule, μ_{ORG}, are defined as:

$$\mu_M = -WF \quad (3)$$

$$\mu_{ORG} = -(IP - EA)/2 \quad (4)$$

where IP and EA are the ionization potential and electron affinity, respectively. The chemical potential of Au and **BTTh** are 4.75 eV and 3.987 eV, respectively.

Charge is transferred from the species with higher chemical potential to the one with lower chemical potential, *i.e.* from Au film to **BTTh**.[87,88] Moreover, since HOMO of **BTTh** is at lower energy than the Au Fermi level (IP > WF), Au will donate electrons to **BTTh**.[75]

4. Conclusions

We designed and prepared small organic molecule–Au NPs hybrids by anchoring the **BTTh** molecule *via* –SH end groups to Au NPs with size in the range 30–120 nm, comparing them with **BTTh** on Au film and glass. We found that Au NPs with size ≤70 nm form uniform monolayers with high intra- and interchain order and high molecular density thanks to the role of the –SH end group anchoring the gold. Our experimental analysis also demonstrated that charge transfer between **BTTh** and Au NPs occurs only for size ≤70 nm.

Combining ellipsometric, Raman and PL measurements with HOMO/LUMO data from CV and WFs from KPFM, we

constructed the scheme of the energy levels at the interface **BTTh**/Au NPs to rationalize the right energy level alignment in order to promote an efficient charge transfer.

Our work highlights how it is possible to forecast and control the direction of the metal-induced charge transfer in different organic molecule–metal NPs hybrids, providing a useful tool to optimize the emission properties of organic emitters.

Conflicts of interest

There are no conflicts to declare.

Data availability

All data supporting the findings of this study are available within the article.

Acknowledgements

This research received funding from (a) the European Union's Horizon 2020 research and innovation programme under grant agreement No 899598—PHEMTRONICS and (b) MUR, project PON ARS01_00951_V0584, D.D.n. 2051 del 02/08/2018, titled: "ECOTEC – Smart and eco-sustainable fibres and tissues for technical clothing and high fashion". We acknowledge our collaborator Sig. Alberto Sacchetti for assistance in performing the experiments.

References

1 T. Mokari, E. Rothenberg, I. Popov, R. Costi and U. Banin, *Science*, 2004, **304**, 1787–1790.
2 L. Carbone and P. D. Cozzoli, *Nano Today*, 2010, **5**, 449–493.
3 R. Costi, A. E. Saunders and U. Banin, *Angew. Chem., Int. Ed.*, 2010, **49**, 4878–4897.
4 T. Mokari, *Nano Rev.*, 2011, **2**, 5983.
5 A. Vaneski, A. S. Susha, J. Rodriguez-Fernandez, M. Berr, F. Jaeckel, J. Feldmann and A. L. Rogach, *Adv. Funct. Mater.*, 2011, **21**, 1547–1556.
6 M. Fahlman, M. Loegdlund, S. Stafstroem, W. R. Salaneck, R. H. Friend, P. L. Burn, A. B. Holmes, K. Kaeriyama, Y. Sonoda, O. Lhost, F. Meyers and J. L. Bredas, *Macromolecules*, 1995, **28**, 1959–1965.
7 M. Fahlman, D. D. Gebler, N. Piskun, T. M. Swager and A. J. Epstein, *J. Chem. Phys.*, 1998, **109**, 2031–2037.
8 G. Hadziioannou and G. G. Malliaras, *Semiconducting Polymers: Chemistry, Physics and Engineering*, Wiley-Vch, Weinheim, 2nd edn, 2007, pp. 1–68.
9 S. Reineke, F. Lindner, G. Schwartz, N. Seidler, K. Walzer, B. Lussem and K. Leo, *Nature*, 2009, **459**, 234–238.
10 M. J. Malachowski and J. Zmija, *Opto-Electron. Rev.*, 2010, **18**, 121–136.
11 P. W. M. Blom, V. D. Mihailetchi, L. J. A. Koster and D. E. Markov, Device Physics of Polymer: Fullerene Bulk Heterojunction Solar Cells, *Adv. Mater.*, 2007, **19**, 1551–1566.
12 M. Gratzel, Solar cells to dye for, *Nature*, 2003, **421**, 586–587.
13 P. Lin and F. Yan, *Adv. Mater.*, 2012, **24**, 34–51.
14 M. C. Scharber and N. S. Sariciftci, *Prog. Polym. Sci.*, 2013, **38**, 1929–1940.
15 W. Brütting, *Physics of Organic Semiconductors*, Wiley-VCH Verlag GmbH&Co., Weinheim, 2013, pp. 1–623.
16 E. Goiri, P. Borghetti, A. El-Sayed and J. E. Ortega, *Adv. Mater.*, 2016, **28**, 1340–1368.
17 H. Ishii, K. Sugiyama, E. Ito and K. Seki, *Adv. Mater.*, 1999, **11**, 605–625.
18 S. Braun, W. R. Salaneck and M. Fahlman, *Adv. Mater.*, 2009, **21**, 1450–1472.
19 C. D. Dimitrakopoulos and P. R. L. Malenfant, *Adv. Mater.*, 2002, **14**, 99–117.
20 C. Vijayakumar, B. Balan, A. Saeki, T. Tsuda, S. Kuwabata and S. Seki, *J. Phys. Chem. C*, 2012, **116**, 17343–17350.
21 P. M. Beaujuge, J. Subbiah, K. R. Choudhury, S. Ellinger and T. D. McCarley, *Chem. Mater.*, 2010, **22**, 2093–2106.
22 P. Ledwon, P. Zassowski, T. Jarosz, M. Lapkowski, P. Wagner, V. Cherpakd and P. Stakhirad, *J. Mater. Chem. C*, 2016, **4**, 2219–2227.
23 Y. Jeon, T. M. Kim, J. J. Kim and J. I. Hong, *New J. Chem.*, 2015, **39**, 9591–9595.
24 K. H. Ong, S. L. Lim, J. Li, H. K. Wong, H. S. Tan, T. T. Lin, L. C. H. Moh, J. C. de Mello and Z. H. Chen, *Polym. Chem.*, 2013, **4**, 1863–1873.
25 B. Lim, J. Jo, D. Khim, H. G. Jeong, B. K. Yu, J. Kim and D. Y. Kim, *Org. Electron.*, 2010, **11**, 1772–1778.
26 L. Sun, F. Q. Bai, Z. X. Zhao and H. X. Zhang, *Sol. Energy Mater. Sol. Cells*, 2011, **95**, 1800–1810.
27 M. Karakus, D. H. Apayd, D. E. Yıldız, L. Toppare and A. Cirpan, *Polymer*, 2012, **53**, 1198–1202.
28 A. Cardone, C. Martinelli, M. Losurdo, E. Dilonardo, G. Bruno, G. Scavia, S. Destri, P. Cosma, L. Salamandra, A. Reale, A. Di Carlo, A. Aguirre, B. Milián-Medina, J. Gierschner and G. M. Farinola, *J. Mater. Chem. A*, 2013, **1**, 715–727.
29 A. Cardone and A. L. Capodolupo, *Materials*, 2022, **15**, 6333.
30 J. E. Beesley, in *Colloidal Gold: Principles, Methods and Applications*, ed. M. A. Hayat, Academic Press, San Diego, 1989, vol. 1, pp. 421.
31 C. Yang, Y. Wang, J. L. Marty and X. Yang, *Bioelectronics*, 2011, **26**, 2724–2727.
32 X. P. Liu, Z. H. Zhou, L. L. Zhang, Z. Y. Tan, G. L. Shen and R. Q. Yu, *Chin. J. Chem.*, 2009, **27**, 1855–1859.
33 C. Pang, R. Li, X. Wang, W. Kong and F. Chen, *Laser Photonics Rev.*, 2026, e02571.
34 G. Shakhgildyan, L. Avakyan, G. Atroshchenko, M. Vetchinnikov, A. Zolikova, E. Ignat'eva, M. Ziyatdinova and E. Subcheva, *Ceramics*, 2024, **7**, 562–578.

35 R. Liudvinavićius and E. Stankevićius, *Opt. Mater.*, 2026, **173**, 117873.
36 M. M. Giangregorio, W. Jiao, G. V. Bianco, P. Capezzuto, A. S. Brown, G. Bruno and M. Losurdo, *Nanoscale*, 2015, **7**, 12868–12877.
37 M. M. Giangregorio, M. Losurdo, A. Sacchetti, P. Capezzuto and G. Bruno, *J. Lumin.*, 2006, **121**, 322–326.
38 F. Denat, H. Gaspard-Iloughmane and J. Dubac, *Synthesis*, 1992, 954–956.
39 A. L. Capodilupo, E. Fabiano, L. De Marco, G. Ciccarella, G. Gigli, C. Martinelli and A. Cardone, *J. Org. Chem.*, 2016, **81**, 3235–3245.
40 C. O. Sanchez, P. Sobarzo and N. Gatica, *New J. Chem.*, 2015, **39**, 7979–7987.
41 C. Hendrich, J. Bosbach, F. Stietz, F. Hubenthal, T. Vartanyan and F. Trager, *Appl. Phys. B*, 2003, **76**, 869–875.
42 B. Foerster, V. A. Spata, E. A. Carter, C. Sönnichsen and S. Link, *Sci. Adv.*, 2019, **5**, eaav0704.
43 E. Riedel and C. Janiak, *Anorganische Chemie*, De Gruyter Studium, de Gruyter, 2007, pp. 1–1014.
44 G. Bruno, F. Babudri, A. Operamolla, G. V. Bianco, M. Losurdo, M. M. Giangregorio, O. H. Omar, F. Mavelli, G. M. Farinola, P. Capezzuto and F. Naso, *Langmuir*, 2010, **26**, 8430–8440.
45 S. Sonnichsen, T. Franzl, T. Wilk, G. von Plessen and J. Feldmann, *Phys. Rev. Lett.*, 2002, **88**, 077402.
46 K. Munechika, J. M. Smith, Y. Chen and D. S. Ginger, *J. Phys. Chem. C*, 2007, **111**, 18906–18911.
47 B. Foerster, A. Joplin, K. Kaefer, S. Celiksoy, S. Link and C. Sonnichsen, *ACS Nano*, 2007, **11**, 2886–2893.
48 R. Das, S. Sarkar, M. Saha, P. C. Dey and S. S. Nath, *J. Lumin.*, 2015, **168**, 325–329.
49 M. Pattabi and M. R. Pattabi, *Nano Hybrids*, 2014, **6**, 1–35.
50 H. Liao, W. Wen and G. K. L. Wong, *J. Opt. Soc. Am. B*, 2006, **23**, 2518–2521.
51 J. Zhang, J. Malicka, I. Gryczynski and J. R. Lakowicz, *Anal. Biochem.*, 2004, **330**, 81–86.
52 Y. Zhao, Y. Jiang and Y. Fang, *Spectrochim. Acta, Part A*, 2006, **65**, 1003–1006.
53 A. Longo, G. P. Pepe, G. Carotenuto, A. Ruotolo, S. De Nicola, V. I. Belotelov and A. K. Zvezdin, *Nanotechnology*, 2007, **18**, 565701.
54 U. Kreibig and M. Vollmer, *Optical Properties of Metal Clusters*, Springer Berlin, Heidelberg, 1995, vol. 25, pp. 1–535.
55 O. P. Siwach and P. Sen, *J. Nanopart. Res.*, 2008, **10**, 107–114.
56 N. Nilius, N. Ernst and H. J. Freund, *Phys. Rev. Lett.*, 2000, **84**, 3994–3997.
57 W. P. Halperin, Quantum size effects in metal particles, *Rev. Mod. Phys.*, 1986, **58**, 533–606.
58 B. Varnholt, P. Oulevey, S. Luber, C. Kumara, A. Dass and T. Bürgi, *J. Phys. Chem. C*, 2014, **118**, 9604–9611.
59 A. Tlahuice-Flores, R. L. Whetten and M. Jose-Yacaman, *J. Phys. Chem. C*, 2013, **117**, 12191–12198.
60 C. K. A. Nyamekye, S. C. Weibel and E. A. Smith, *J. Raman Spectrosc.*, 2021, **52**, 1246–1255.
61 N. Sheppard, *Trans. Faraday Soc.*, 1950, **46**, 429–439.
62 F. T. Van, S. Garreau, G. Louarn, G. Froyer and G. C. Chevrot, *J. Mater. Chem.*, 2001, **11**, 1378–1382.
63 W. C. Tsoi, D. T. James, J. S. Kim, P. G. Nicholson, C. E. Murphy, D. D. C. Bradley, J. Nelson and J. S. Kim, *J. Am. Chem. Soc.*, 2011, **133**, 9834–9843.
64 J. Serrano, J. Casado, V. Hernandez, L. Favaretto, G. Destefano and J. T. L. Navarette, *J. Mol. Struct.*, 2001, **563–564**, 539–544.
65 V. Hernandez, F. J. Ramirez, T. F. Otero and J. T. L. Navarette, *J. Chem. Phys.*, 1994, **100**, 114–129.
66 M. Galleya, M. Pravicaa and Z. Liuc, *Research*, 2013, **33**, 40–54.
67 J. Ip, T. P. Nguyen, P. Le Rendu and V. H. Tran, *Synth. Met.*, 2001, **122**, 45–47.
68 G. Louarn, J. P. Buisson, S. Lefrant and D. Fichou, *J. Phys. Chem.*, 1995, **99**, 11399–11404.
69 A. Pron, G. Louarn, M. Lapkowski, M. Zagorska, J. Glowezyk-Zubek and S. Lefrant, *Macromolecules*, 1995, **28**, 4644–4649.
70 C. M. Castro, M. C. R. Delgrado, V. Hernandez, S. Hotta, J. Casado and J. T. Navarrete, *J. Chem. Phys.*, 2002, **116**, 10419–10427.
71 J. L. Zafra, J. Casado, I. I. Perepichka, I. F. Perepichka, M. R. Bryce, F. J. Ramirez and J. T. L. Navarette, *J. Chem. Phys.*, 2011, **134**, 044520.
72 Y. Gao and J. K. Grey, *J. Am. Chem. Soc.*, 2009, **131**, 9654–9662.
73 G. Louarn, J. P. Buisson, S. Lefrant and D. J. Fichou, *Phys. Chem.*, 1995, **99**, 11399–11404.
74 R. Otero, A. L. V. de Parga and J. M. Gallego, *Surf. Sci. Rep.*, 2017, **72**, 105–145.
75 A. Vilan and D. Cahen, *Chem. Rev.*, 2017, **117**, 4624–4666.
76 X. Crispin, V. Geskin, A. Crispin, J. Cornil, R. Lazzaroni, W. R. Salaneck and J. L. Bredas, *J. Am. Chem. Soc.*, 2002, **124**, 8131–8141.
77 S. H. Lee, S. W. Lee, T. Jeon, D. H. Park, S. C. Jung and J. W. Jang, *Nano Energy*, 2019, **63**, 103841.
78 L. Zhou, Q. Huang and Y. Xia, *Chem. Rev.*, 2024, **124**, 8597–8619.
79 C. Jia, X. Li, N. Xin, Y. Gong, J. Guan, L. Meng, S. Meng and X. Guo, *Adv. Energy Mater.*, 2016, **6**, 1600431.
80 B. Foerster, A. Joplin, K. Kaefer, S. Celiksoy, S. Link and C. Sonnichsen, *ACS Nano*, 2017, **11**, 2886–2893.
81 T. Zheng, S. Bott and Q. Huo, *ACS Appl. Mater. Interfaces*, 2016, **8**, 21585–21594.
82 M. Valenti, M. P. Jonsson, G. Biskos, A. Schmidt-Otta and W. A. Smith, *J. Mater. Chem. A*, 2016, **4**, 17891–17912.
83 N. D. Burrows, W. Lin, J. G. Hinman, J. M. Dennison, A. M. Vartanian, N. S. Abadeer, E. M. Grzincic, L. M. Jacob, J. Li and C. J. Murphy, *Langmuir*, 2016, **32**, 9905–9921.
84 S. Sarina, E. Jaatinen, Q. Xiao, Y. M. Huang, P. Christopher, J. C. Zhao and H. Y. Zhu, *J. Phys. Chem. Lett.*, 2017, **8**, 2526–2534.

85 S. A. Lee and S. Link, *Acc. Chem. Res.*, 2021, **54**, 1950–1960.
86 Y. Zhang, S. He, W. Guo, Y. Hu, J. Huang and J. R. Mulcahy, *Chem. Rev.*, 2018, **118**, 2927–2954.
87 R. Otero, A. L. VázquezdeParga and J. M. Gallego, *Surf. Sci. Rep.*, 2017, **72**, 105–145.
88 S. Braun, W. R. Salaneck and M. Fahlman, *Adv. Mater.*, 2009, **21**, 1450–1472.